ChemComm

Check for updates

Construction of a superior visible-light-driven photocatalyst based on a C_3N_4 active centre-photoelectron shift platform-electron withdrawing unit triadic structure covalent organic framework†

Sijing He, [ab] Qinfeng Rong, [c] Hongyun Niu [a] and Yaqi Cai [*abd]

Herein, three functional factors inducing photocatalytic ability were artfully integrated into a covalent organic framework (COF), where triazine units served as photoactive centers, cyclic ketone units served as electron-withdrawing moieties, and the conjugated structure served as a photoelectron shift platform. This COF with segregated donor–acceptor alignments exhibits an excellent visible-light photocatalytic capacity for the decomposition of organic pollutants.

Extensive attention has been paid to the sufficient use of sunlight as a clean and renewable energy source for water decontamination since it subtly alleviates the energy crisis and environmental issues at the same time. Thus, in this regard, the development of an efficient and stable photocatalyst with high visible-light response is crucial. Contrary to traditional TiO_2 inorganic semiconductors, graphitic carbon nitride (g-C_3N_4) possesses a narrower band gap (2.7 eV) and harnesses a broader wavelength range of solar energy, which has gradually attracted attention as a nontoxic metal-free and visible-light-induced photocatalyst.[1] However, the photocatalytic efficiency of pristine bulk g-C_3N_4 depends on its intrinsic chemical structure, which consists of repeated building units; therefore, the photogenerated electrons can hardly transfer from the light-harvesting center. The defects of marginal visible-light absorption and fast charge recombination severely hinder the wide applications of bulk g-C_3N_4.[2] To date, many efforts, including heteroatom doping,[3–7] nanostructure engineering,[8–11] noble metal deposition,[12–16] and semiconductor hybridization,[17–21] have been devoted to promote its photocatalytic performance. However, these strategies involve some tedious synthetic procedures, and the

improvement in photocatalytic efficiency is limited, especially for the degradation of chemically stable organic pollutants,[22] due to the fundamentally insurmountable restriction of the g-C_3N_4 architecture. Therefore, a dramatically enhanced photocatalytic performance of the organic semiconductors is expected to be realized *via* predesigning their molecular structures to tune light harvesting and maneuver charge kinetics.

Herein, we selected a proper electron-deficient monomer in combination with the visible-light catalytic active substituent C_3N_4 to fabricate a new covalent organic framework (COF) photocatalyst, whose conjugated system served as a photoelectron shift platform. This ingenious design can effectively modulate the electronic band structure to reduce the band gap and positive-shift the valence band (VB) position, thereby resulting in enhanced light-harvesting capability and photooxidation property. Moreover, the ordered donor–acceptor structure in the COF boosts the efficiency of the photoinduced electron transfer and charge separation. As expected, this COF exhibited remarkable photocatalytic activity towards the purification of water under visible light, far outperforming the bulk g-C_3N_4. Furthermore, this photocatalyst was fairly stable even after repeated cycling. This study will provide a new approach for the structural design of organic semiconductors at a molecular level.

A novel C_3N_4 active center inlaid COF (denoted as TpMA) was successfully synthesized under solvothermal conditions *via* the co-condensation of 1,3,5-triformylphloroglucinol (Tp) and melamine (MA). The TpMA formation proceeds through a two-step path (Fig. 1a): the first step involves a reversible Schiff-base reaction, and the second step involves an irreversible enol–keto tautomerization, which renders TpMA superior chemical stability towards water, acids, and bases. The resulting powder was initially verified by elemental analysis, Fourier transform infrared (FT-IR) spectroscopy, and solid-state nuclear magnetic resonance (NMR) spectroscopy. The elemental analysis results indicated the following approximate values for the composition of TpMA: C (49.20%), H (4.12%), N (30.07%), and O (16.83%); these values are largely in agreement with the theoretical values for an infinite 2D sheet (calculated for $C_{12}H_6N_6O_3$: C 51.07%, H 2.14%, N 29.78%, and

[a] State Key Laboratory of Environmental Chemistry and Ecotoxicology, Research Center for Eco-Environmental Sciences, Chinese Academy of Sciences, Beijing 100085, China. E-mail: caiyaqi@rcees.ac.cn

[b] University of Chinese Academy of Sciences, Beijing 100049, China

[c] Key Laboratory of Bio-Inspired Smart Interfacial Science and Technology of Ministry of Education, School of Chemistry, Beihang University, Beijing 100191, China

[d] Institute of Environment and Health, Jianghan University, Wuhan 430056, China

† Electronic supplementary information (ESI) available: Additional experimental details and figures. See DOI: 10.1039/c7cc04515h
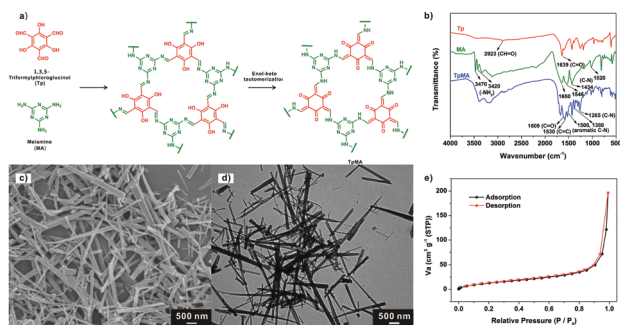
Communication

Fig. 1 (a) Schiff base reaction followed by irreversible enol-to-keto tautomerization of TpMA; (b) FT-IR spectra of Tp, MA and TpMA; (c) SEM image, (d) TEM image, and (e) N_2 adsorption–desorption isotherm of TpMA.

Fig. 2 (a) Photocatalytic degradation of MO ($10~mg~L^{-1}$) over $g-C_3N_4$ and TpMA under visible light irradiation; (b) UV-visible absorption spectra of MO at different irradiation times obtained using TpMA.

O 17.01%). The FT-IR spectra of TpMA (Fig. 1b) featured bands at $1578~cm^{-1}$ and $1265~cm^{-1}$, ascribed to the stretching vibrations of C=C and C–N, respectively, whereas the aromatic C–N stretching band, characteristic of the triazine units, emerged at around $1508~cm^{-1}$ and $1380~cm^{-1}$. These results are indicative of the successful formation of TpMA. Solid-state 13C cross-polarization magic-angle spinning (CP-MAS) NMR spectrum further supported the keto form of TpMA and confirmed the existence of triazine rings in the framework (Fig. S1 in ESI†). The field emission scanning electron microscopy (FE-SEM) and transmission electron microscopy (TEM) images of TpMA showed a thread-like morphology with an average width of 60–180 nm (Fig. 1c and d). The powder X-ray diffraction (PXRD) pattern of TpMA (Fig. S2, ESI†) indicates a framework with certain structural orderliness, based on the multiple peaks in the 2θ range from 3 to 35°.[23]

The chemical composition and elemental states of TpMA were determined by X-ray photoelectron spectroscopy (XPS). As shown, the survey XPS spectrum of TpMA confirms the coexistence of the elements C, N, and O in the sample (Fig. S3a, ESI†). The high resolution spectrum of C 1s (Fig. S3b, ESI†) can be deconvoluted into three individual components located at 284.6, 286.6, and 288.5 eV, corresponding to sp^2 C=C, C=O, and N–C=N bonds, respectively. The N 1s spectrum (Fig. S3c, ESI†) can be fitted into two peaks, which are assigned to sp^2-hybridized nitrogen in triazine rings (C–N=C, 398.8 eV) and amino functional groups (C–N–H, 400.5 eV). TpMA displayed identical thermal stability up to 300 °C (Fig. S4, ESI†), as revealed by thermogravimetric analysis (TGA). The N_2 adsorption isotherm acquired at 77 K for TpMA appeared as a typical type-I isotherm (Fig. 1e), which indicated a permanent microporous nature. The Brunauer–Emmett–Teller (BET) surface area of TpMA was found to be $56.9~m^2~g^{-1}$.

The disposal of organic dyes from industry into water bodies causes deteriorating environmental problems due to their high toxicity, carcinogenicity, and non-biodegradability. Methyl orange (MO, an azo dye) is quite stable under visible light illumination without the addition of a photocatalyst, and its self-photolysis can be neglected. Herein, we chose MO as a model contaminant to evaluate the visible-light-driven photocatalytic performance of synthesized TpMA. Prior to the photodegradation test, dark absorption tests were conducted by placing the photocatalysts
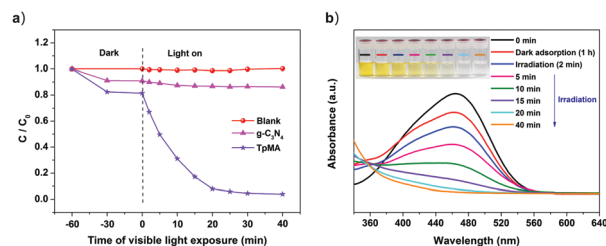
in contact with the organic dye solution in the dark for 1 h. The variation in the MO concentration was monitored during the whole process. As presented in Fig. 2a, the adsorption tended to saturate, with adsorption ability reaching and not exceeding 18.5%; this demonstrates that the complete disintegration of dye over TpMA under irradiation is mainly attributed to photocatalysis rather than adsorption. Notably, it can be observed that TpMA exhibits a superior MO photodegradation capacity as compared to bulk $g-C_3N_4$. After 40 min irradiation with visible light, TpMA could completely degrade the MO solution (Fig. 2b), whereas almost no decolorization of MO was observed in the presence of pure bulk $g-C_3N_4$. Even on elongating the exposure time to 6 h, only about 33.5% MO dye molecules were decomposed over bulk $g-C_3N_4$. Total organic carbon (TOC) measurements further confirmed that a 36.7% of mineralization of MO was achieved after a 40 min-irradiation over TpMA. Furthermore, the MO photocatalytic degradation over TpMA obeys pseudo-first-order kinetics, that is, $-\ln(C/C_0) = kt$, where k is the rate constant, and C and C_0 are the actual and initial concentrations of MO, respectively. As shown in Fig. S5 (ESI†), TpMA displayed a faster reaction rate for the degradation of MO with an apparent kinetic constant of $1.02 \times 10^{-1}~min^{-1}$, which is about 59 times enormously higher than that for $g-C_3N_4$ ($1.72 \times 10^{-3}~min^{-1}$). Besides the MO dye, a colorless organic pollutant, phenol, has also been utilized to assess the photocatalytic capability of TpMA. As observed from Fig. S6 (ESI†), a similar photocatalytic degradation trend was attained with phenol: 90% of phenol was photodegraded with TpMA after 40 min – irradiation as compared to only 8% with $g-C_3N_4$.

The investigations on the optical and electronic properties of TpMA are favorable to better understand the origin of its photocatalytic activity. UV-vis diffuse reflectance spectra (DRS) of bulk $g-C_3N_4$ and TpMA samples are shown in Fig. 3a. $g-C_3N_4$ presents the typical absorption patterns of semiconductors. For TpMA, the absorption edge was red-shifted, and the optical absorption was enhanced across the entire tested wavelength range. It is evident that TpMA has an absorption shoulder occurring at 520 nm in the visible light region. The band gap energies (E_g) of bulk $g-C_3N_4$ and TpMA were estimated to be 2.70 and 2.30 eV, respectively. The narrower band gap of TpMA allows to absorb more visible-light photons to activate more photogenerated charge carriers participating in the photocatalytic process. The band structures of the two samples were further examined by valence band X-ray photoelectron
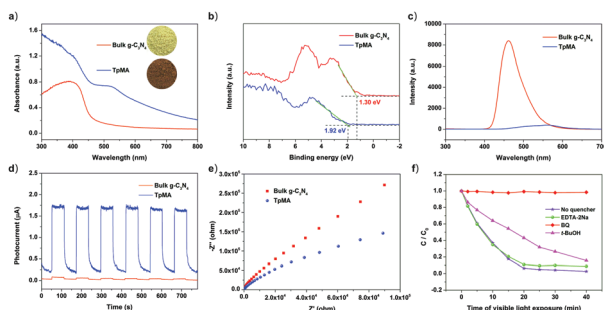
Fig. 3 (a) UV-vis diffuse reflectance spectra, (b) VB XPS spectra, (c) photoluminescence spectra, (d) photocurrent responses, and (e) EIS Nyquist plots of bulk g-C_3N_4 and TpMA; (f) photodegradation of MO over TpMA in the presence of different scavengers.

Fig. 4 Schematic of the band gap structures of bulk g-C_3N_4 and TpMA, and the proposed photocatalytic mechanism for the degradation of MO and phenol over TpMA under visible light irradiation.

spectroscopy (VB XPS). From Fig. 3b, the VB edge of TpMA is determined to be 1.92 eV, which is more positive than that of g-C_3N_4 (1.30 eV). This feature endows TpMA with a stronger photooxidation capability for pollutant degradation. Based on the band gap values, conduction band (CB) positions of bulk g-C_3N_4 and TpMA are calculated to be −1.40 eV and −0.38 eV, respectively.

The efficient generation, separation, and migration of photoexcited electron–hole pairs are a prerequisite to initiate a photocatalytic reaction, which can be analyzed by photoluminescence (PL) emission spectroscopy, photoelectrochemical tests, and electrochemical impedance spectroscopy (EIS). As shown in Fig. 3c, the PL intensity of TpMA is far weaker than that of bulk g-C_3N_4; this suggests a suppressed recombination of the photogenerated carriers. Fig. 3d depicts the transient photocurrent responses of bulk g-C_3N_4 and TpMA with several on–off cycles of intermittent illumination. The photocurrent response of TpMA is steady and shows no decay, being approximately 22-fold higher than that of bulk g-C_3N_4, indicating a lower recombination rate and improved charge carrier mobility. Moreover, in comparison with bulk g-C_3N_4, a smaller arc radius on the EIS Nyquist plot of TpMA represents a faster interfacial charge transfer (Fig. 3e), which is consistent with the tendency of the PL spectra and photocurrent responses. Based on these results, it is quite reasonable to conclude that the incorporation of the electron-withdrawing Tp monomer into the polymer network greatly facilitates the spatial separation of charge carriers upon photoexcitation and inhibits their recombination. Besides this, the infinitely extended 2D conjugated structure of TpMA leads to enhanced electronic delocalization, which is conducive to the transfer and mobility of carriers along the layers. All these superiorities and the desirable electronic band structure of TpMA are responsible for its superb photocatalytic activity.

To elucidate the photocatalytic mechanism of TpMA, trapping experiments were performed to study the roles of possible reactive species in photocatalysis. Scavengers such as *tert*-butanol (*t*BA), *p*-benzoquinone (BQ), and ethylenediaminetetraacetic acid disodium salt (EDTA-2Na) were applied to quench hydroxyl radicals (OH$^-$), superoxide radicals (O$_2{}^-$), and holes (h$^+$), respectively. As shown in Fig. 3f, the MO decomposition over TpMA was completely suppressed with the addition of BQ, whereas the photodegradation efficiency of MO was slightly decreased in the presence of *t*BA.
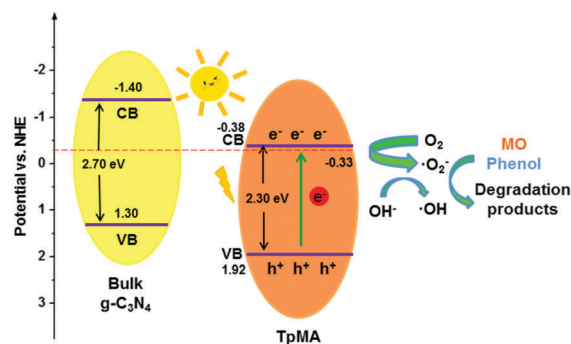
By contrast, EDTA-2Na had virtually no effect on the degradation of the model pollutant. Accordingly, it can be concluded that the photodegradation of MO is driven by the contribution of O$_2{}^-$ radicals with the assistance of OH$^-$.

On the basis of the abovementioned analyses, the underlying photocatalytic mechanism of TpMA has been proposed and illustrated in Fig. 4. When irradiated with the photons of energy exceeding (or equal to) the band gap of TpMA ($E \geq 2.30$ eV or $\lambda \leq 539$ nm), excess electrons and holes could be formed in the highly delocalized conjugated system of TpMA. The photoinduced electrons are injected into the CB of TpMA, leaving holes in the VB. Subsequently, the enriched electrons in the CB are captured by the dissolved O$_2$ to yield abundant O$_2{}^-$ (E^0, O$_2$/O$_2{}^-$ = −0.33 eV vs. NHE),[24–26] and then, O$_2{}^-$ radicals react with H$_2$O to further produce active OH$^-$. These generated reactive oxygen species (O$_2{}^-$ and OH$^-$) can effectively oxidize and mineralize the MO molecules owing to their high oxidative capacity.

In addition to photocatalytic activity, the stability of a photocatalyst is another desirable feature for practical application. Herein, four consecutive experiments using TpMA as a photocatalyst were carried out to evaluate its stability for MO degradation. As it is evident from Fig. S7 (ESI†), a negligible deactivation of TpMA appeared after recycling four times, whereas TpMA still retained a photocatalytic ability of 86.8%. This confirms that TpMA can be effectively recycled for repeated photocatalytic cycles without any major loss of activity. No significant differences were observed in the chemical structure or in the morphology of TpMA after dye photodecomposition, as further verified by FT-IR and TEM analysis (Fig. S8 and S9, ESI†). The outstanding stability of TpMA is inextricably linked to its chemical architecture, where proton tautomerism endows the framework with exceptional stability.

In summary, herein, for the first time, a C$_3$N$_4$ constituent inlaid COF was designed and synthesized, where triazine units acted as the photoactive centers, cyclic ketone units acted as electron-withdrawing moieties, and the conjugated structure acted as a photoelectron shift platform. Subsequently, the photoelectric properties and photocatalytic performance of the as-prepared TpMA and pristine bulk g-C$_3$N$_4$ were systematically investigated and compared. The results suggest that TpMA exhibits superior visible light photocatalytic ability in eliminating organic contaminant.

The intrinsic electronic structure was tuned by the incorporation of electron-deficient monomers, such that light absorption and photooxidation capability were enhanced. Moreover, the interdigitated donor–acceptor heterojunctions could effectively promote charge separation upon photoexcitation. We envisage that this strategy will offer a feasible approach towards the design and construction of highly efficient visible-light-induced photocatalysts with desired band structures.

Conflicts of interest

There are no conflicts to declare.

Notes and references

1 X. Wang, K. Maeda, A. Thomas, K. Takanabe, G. Xin, J. M. Carlsson, K. Domen and M. Antonietti, *Nat. Mater.*, 2009, **8**, 76–80.
2 T. Xiong, W. Cen, Y. Zhang and F. Dong, *ACS Catal.*, 2016, **6**, 2462–2472.
3 Y. Zhu, T. Ren and Z. Yuan, *ACS Appl. Mater. Interfaces*, 2015, **7**, 16850–16856.
4 Y. Wang, J. Zhang, X. Wang, M. Antonietti and H. Li, *Angew. Chem., Int. Ed.*, 2010, **49**, 3356–3359.
5 Y. Wang, H. Wang, F. Chen, F. Cao, X. Zhao, S. Meng and Y. Cui, *Appl. Catal., B*, 2017, **206**, 417–425.
6 J. Li, B. Shen, Z. Hong, B. Lin, B. Gao and Y. Chen, *Chem. Commun.*, 2012, **48**, 12017–12019.
7 G. Liu, P. Niu, C. Sun, S. C. Smith, Z. Chen, G. Q. Lu and H. Cheng, *J. Am. Chem. Soc.*, 2010, **132**, 11642–11648.
8 Z. Tong, D. Yang, Z. Li, Y. Nan, F. Ding, Y. Shen and Z. Jiang, *ACS Nano*, 2017, **11**, 1103–1112.
9 P. Niu, L. Zhang, G. Liu and H. Cheng, *Adv. Funct. Mater.*, 2012, **22**, 4763–4770.
10 M. Tahir, C. Cao, F. K. Butt, F. Idrees, N. Mahmood, Z. Ali, I. Aslam, M. Tanveer, M. Rizwan and T. Mahmood, *J. Mater. Chem. A*, 2013, **1**, 13949–13955.
11 X. Jin, V. V. Balasubramanian, S. T. Selvan, D. P. Sawant, M. A. Chari, G. Q. Lu and A. Vinu, *Angew. Chem.*, 2009, **121**, 8024–8027.
12 J. Zhang, X. Chen, K. Takanabe, K. Maeda, K. Domen, J. D. Epping, X. Fu, M. Antonietti and X. Wang, *Angew. Chem., Int. Ed.*, 2010, **49**, 441–444.
13 X. Wang, X. Chen, A. Thomas, X. Fu and M. Antonietti, *Adv. Mater.*, 2009, **21**, 1609–1612.
14 S. Martha, A. Nashim and K. M. Parida, *J. Mater. Chem. A*, 2013, **1**, 7816–7824.
15 G. Zhang, C. Huang and X. Wang, *Small*, 2015, **11**, 1215–1221.
16 S. Samanta, S. Martha and K. Parida, *ChemCatChem*, 2014, **6**, 1453–1462.
17 S. Le, T. Jiang, Y. Li, Q. Zhao, Y. Li, W. Fang and M. Gong, *Appl. Catal., B*, 2017, **200**, 601–610.
18 D. Zheng, G. zhang and X. Wang, *Appl. Catal., B*, 2015, **179**, 479–488.
19 S. Kumar, A. Baruah, S. Tonda, B. Kumar, V. Shanker and B. Sreedhar, *Nanoscale*, 2014, **6**, 4830–4842.
20 S. Pany and K. M. Parida, *Phys. Chem. Chem. Phys.*, 2015, **17**, 8070–8077.
21 S. Nayak, L. Mohapatra and K. Parida, *J. Mater. Chem. A*, 2015, **3**, 18622–18635.
22 J. Xiao, Y. Xie, F. Nawaz, S. Jin, F. Duan, M. Li and H. Cao, *Appl. Catal., B*, 2016, **181**, 420–428.
23 Y. Du, H. Yang, J. M. Whiteley, S. Wan, Y. Jin, S.-H. Lee and W. Zhang, *Angew. Chem., Int. Ed.*, 2016, **55**, 1737–1741.
24 S. Wang, D. Li, C. Sun, S. Yang, Y. Guan and H. He, *Appl. Catal., B*, 2014, **144**, 885–892.
25 X. Yang, F. Qian, G. Zou, M. Li, J. Lu, Y. Li and M. Bao, *Appl. Catal., B*, 2016, **193**, 22–35.
26 S. Kumar, A. Baruah, S. Tonda, B. Kumar, V. Shanker and B. Sreedhar, *Nanoscale*, 2014, **6**, 4830–4842.